Korean J. Chem. Eng., 36(3), 393-403 (2019)
DOI: 10.1007/s11814-018-0187-5

pISSN: 0256-1115
eISSN: 1975-7220

Impact of pressure on the carbon structure of char during pyrolysis of bituminous coal in pressurized entrained-flow reactor

Arash Tahmasebi[*,], Kristina Maliutina[*], and Jianglong Yu[*,**,†]**

*Key Laboratory of Advanced Coal and Coking Technology of Liaoning Province, School of Chemical Engineering, University of Science and Technology Liaoning, Anshan 114051, China
**Chemical Engineering, University of Newcastle, Callaghan, NSW 2308, Australia
(*Received 31 May 2018 • accepted 14 November 2018*)

Abstract−The impact of pressure on the carbon structure of a Chinese bituminous coal was investigated using a pressurized entrained-flow reactor in the temperature and pressure ranges of 700-900 °C and 0.1-4.0 MPa, respectively. Pyrolysis pressure had a significant influence on the physiochemical and carbon structure of chars. The specific surface area and the swelling ratio of chars reached their highest values at 1.0 MPa. Fourier transform infrared spectroscopy (FTIR) analysis showed that higher pressures enhanced the decomposition of functional groups in chars. Raman spectroscopy analysis results revealed that at elevated pressures, the organic matrix and functional groups were removed from the char structure, leading to higher ordering of the carbon structure. During X-ray diffraction (XRD) analysis, parameters such as the stacking height (L_c), interlayer spacing (d_{002}) and lateral size of the graphite structures (L_a) were used to evaluate the graphitic structures in chars. The results showed an increase in L_c, L_a, and the average number of graphene sheets with pyrolysis pressure, indicating a more ordered carbon structure at elevated pressures. The *d*-spacing of char was in the range of 3.34-3.37 Å, similar to typical graphitic structures.

Keywords: Pressurized Entrained-flow Pyrolysis, Carbon Structure, Raman Spectroscopy, Bituminous Coal, Carbon Materials

INTRODUCTION

As the conventional use of coal for power generation becomes increasingly less attractive due to its contribution to CO_2 emissions, smog formation, and global warming, new coal conversion concepts and technologies need to be developed for efficient utilization of abundant coal resources. These issues are especially critical for countries that rely heavily on coal as the primary source of energy. Production of coal-derived carbon materials as an alternative to coal combustion has been recognized as one of the promising methods for efficient and value-added utilization methods of coal. Coal-derived carbon materials may become a valuable source for the production of cost-effective electrode materials [1]. Synthesis of carbon materials from coal has previously been reported in the literature [2-5]. Relatively high surface area and electrical conductivity of carbonized coal chars make them suitable as precursors for electrode materials in Li- and Ca-ion batteries [6,7] and direct carbon fuel cells [8,9]. These applications are reliant on the physiochemical and structural properties of chars such as carbon content, surface area, carbon order, electrical conductivity, and morphology of chars developed during pyrolysis/carbonization [10]. These properties are strongly influenced by the pyrolysis/carbonization process conditions such as final temperature, particle heating rate, and pressure. Although the influence of pyrolysis temperature and heating rate on the development of the char structure has been extensively reported in the literature, a detailed understanding of the impact of pressure on devolatilization and development of carbon structure of char during pyrolysis has not been achieved.

Pyrolysis pressure has a profound impact on the physiochemical structure of char, therefore affecting its reactivity [11,12]. Wire-mesh reactors [13,14], thermogravimetric analyzer (TGA) [15-18], fixed-bed reactor [19], drop tube reactors [20,21], and pressurized entrained-flow reactor [22] have been used to investigate the influence of pressure. Pressure may cause swelling and alter the physical structure of char [20,21,23]. Higher pyrolysis pressures may lead to the formation of chars with lower surface area [12]. However, the porous structure of char may also be affected by its rank and pyrolysis conditions of temperature, heating rates, and particle residence times [15,20]. Tremel et al. [24] reported that the surface area of chars decreased at elevated pressures. Roberts et al. [25] observed that CO_2 surface area of chars reached a maximum value at 10 atm and decreased thereafter, while, N_2 adsorption surface area of chars showed a direct relationship with pyrolysis pressure. Zeng et al. [12], on the other hand, reported an indirect relationship between the surface areas of chars and pyrolysis pressure. Howaniec [15] used a pressurized TGA for pyrolysis of coal and observed that the surface area of chars reached the highest value at 3.0 MPa. The variation of these trends can be attributed to the difference in experimental conditions and the properties of raw materials used in these studies.

Pyrolysis pressure may also affect the carbon structure of char, which can be characterized by using a number of analytical methods such as high-resolution transmission electron microscopy (HRTEM), X-ray diffraction (XRD), and Raman spectroscopy. Raman spectroscopy and XRD provide structural information about char, which

†To whom correspondence should be addressed.
E-mail: jianglong.yu@newcastle.edu.au

allows characterization of carbonaceous materials [19,26]. Char structure evolution during pyrolysis at 300-1,000 °C and 2,600 °C has been reported by Chabalala et al. [27] and Zaida et al. [28]. They showed that chars prepared at temperatures as low as 600 °C have already developed ordered carbonaceous structures. Sheng [29] used Raman spectroscopy to investigate the changes in the microstructure of coal chars generated in a horizontal tube furnace, muffle furnace, and drop tube furnace at temperatures of 910-1,500 °C. It was observed that the structural order of char increased at higher pyrolysis temperatures. Xiao et al. [30] used XRD to investigate the carbon structure of chars prepared during high-temperature pyrolysis and reported that the carbon crystallite structure of coal char became more ordered with the increase of the temperature from 1,000 °C to 1,600 °C. The majority of these studies used chars prepared at atmospheric pressure and literature data on the impact of pressure on the carbon structure of chars are scarce.

A better understanding of the evolution of char structure during pyrolysis is necessary for the development of efficient technologies for the production of coal-based advanced carbon materials. Although significant advancement is achieved in the understanding of the structural evolution of char during pyrolysis, the major focus has been on the physical structure development and subsequent impacts on the gasification and combustion reactivity. However, the influence of pyrolysis conditions, in particular pressure, on the carbon structure of chars has not been fully understood. Therefore, rather than focusing on char reactivity, this study was conducted to gain insight into the impact of pressure on the carbon structure evolution of pyrolysis chars as precursors for coal-based carbon materials. Pyrolysis experiments were carried out at pressures of 0.1-4.0 MPa and temperatures of 700-900 °C using a pressurized entrained-flow reactor. The changes in char structure at elevated pressures were systematically investigated by using analytical techniques such as FTIR, Brunauer-Emmett-Teller (BET) surface area, Raman spectroscopy, and XRD. The potential applications of the chars prepared under pressurized pyrolysis conditions were also proposed and discussed.

MATERIALS AND METHODS

1. Coal Sample Preparation

A bituminous coal from Shanxi Province of China was ground and sieved to a particle size range of 75-125 μm. The properties of the coal sample are shown in Table 1. Before pyrolysis experiments, the coal samples were dried at 105 °C for 24 h to remove the moisture from the coal sample.

2. Pressurized Entrained-flow Pyrolysis Experiments

A new pressurized entrained-flow reactor was used for investigating the high-pressure pyrolysis behavior of coal (Fig. 1). The experimental setup was designed for investigating pyrolysis of solid fuels at operating pressures and temperatures as high as 7.0 MPa and 900 °C, respectively. Argon was used as the carrier gas during pressurized pyrolysis experiments. The experimental setup consisted of four sections: (1) gas supply system, (2) electrically heated entrained-flow reactor with feeding system and a char collector, (3) pyrolysis gas treatment including condensation system, and (4) pressure control with a subsequent gas exhaust system. The sample feeding system was comprised of a hopper and a screw feeder, which allowed a feeding rate in the range of 0.5-6.44 g/min. The feed gas was separated into two streams before the preheater. One stream passed through the hopper to avoid any contact between pyrolysis gas and the raw sample. The second gas stream passed through gas preheater (set at 350 °C) and entered the reactor directly above the heating section.

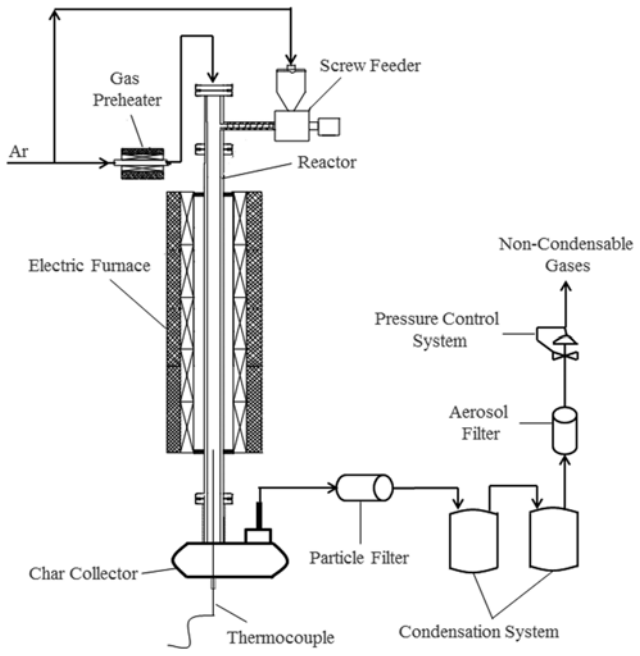

Fig. 1. Schematic diagram of the pressurized entrained-flow reactor for coal pyrolysis.

The entrained-flow reactor with an inner diameter of 14 mm was heated in an electric furnace comprised of five heating zones, each with a length of 300 mm, leading to a total heating zone of 1,500 mm. The char collector, which is located at the bottom of the reactor, was electrically heated to 250 °C to prevent the condensation of volatiles. After leaving the char collector, the process gas, consisting of purge gas and pyrolysis volatiles, passed through the particle filter and subsequently a two-stage condensation system. The non-

Table 1. Proximate and ultimate analysis of pulverized bituminous coal sample

Proximate analysis in wt%				Ultimate analysis in wt% (daf)					HHV (MJ/kg)	FSI	Fluidity (ddpm)
M (ar)	Ash (db)	VM (db)	FC (db)	C	H	N	S	O*			
5.4	7.02	20.56	72.42	70.15	3.08	2.49	1.49	22.78	24.77	4.37	6800

*By difference; FSI: Free Swelling Index

Table 2. Gas temperatures at the outlet of the entrained-flow reactor as a function of operating pressure and temperature

Reactor wall temperature	Outlet gas temperature (°C)			
	0.1 MPa	1.0 MPa	2.0 MPa	4.0 MPa
600 °C	599	584	585	584
700 °C	698	689	681	676
800 °C	794	794	786	776
900 °C	896	890	886	881

condensable gases passed through a pressure control system before being exhausted.

Pyrolysis experiments were carried out at 700, 800, and 900 °C and pressures of 0.1, 1.0, 2.0, and 4.0 MPa. Temperatures of higher than 700 °C were used in this study to ensure that pyrolysis reactions were completed [31-33]. This is particularly important when char is further used as precursors for production of carbon materials. The reactor and the feeder were purged with the carrier gas for an hour prior to each experimental run. The outlet gas was analyzed by an online flue gas analyzer (Tesco 350) to ensure that an oxygen-free environment was achieved. The temperature of the gas at the reactor outlet was measured during preliminary blank experiments by a K type thermocouple inserted into the reactor from the bottom (Fig. 1), and the results are shown in Table 2. As seen, the outlet gas temperature generally followed the reactor wall temperature. A slight decrease of around 20 °C in gas temperature was observed at higher pressures, owing to the lower thermal conductivity of the gas at elevated pressures. For each experimental run, about 20 g of dried coal sample was used. Before each experiment, the temperature of the gas pre-heater and trace heating for char collector was set at 350 and 250 °C, respectively. The reactor was then pressurized to the desired value. Once the reactor temperature and pressures reached a stable value and the reactor was purged for 1 h, the coal feeding at a rate of 0.5 g/min was initiated. This low feeding rate was selected to achieve a dilute phase and single particle heating conditions, where the interaction between the coal particles during heating is minimized. Once the experimental run was completed, the reactor was depressurized and the heating was switched off.

In this study, the stationary particle velocity was calculated according to the approach of Haider and Levenspiel [34]. The drag coefficient in the reactor was a function of sphericity and the Reynolds number of particles and had a direct relationship with the acceleration due to gravity. The superficial gas velocity was calculated from the flow rate of the carrier gas and the cross-section area of the reactor. The slip velocity of coal particles was then calculated as the sum of the stationary particle velocity and the superficial gas velocity [35]. Under the current experimental conditions, the residence time of the coal particle inside the heating zone of the reactor was calculated to be around 4 s.

3. Characterization of Chars

The yield of volatile matter during pyrolysis was determined using the ash tracer method [12]. The swelling ratio of char particles was calculated from the mean particle size of chars to that of the feed coal (d/d_0). The surface morphology of chars was analyzed using scanning electron microscopy (SEM, ZEISS Sigma HD). The internal surface area of char samples was measured by isothermal N_2 adsorption using a specific surface area and pore size analyzer (Vsorb 4800 P). The surface area of chars was calculated by the Brunauer-Emmett-Teller (BET) equation using N_2 adsorption isotherms.

The chemical structure of coal and chars samples prepared under different pyrolysis conditions was analyzed using a Thermo Fisher Nicolet IS5 mid-FTIR spectrometer. Sample pellets were prepared by finely grinding 1.5 mg of coal/char sample with 150 mg KBr.

The development of the carbon structure as a function of pyrolysis conditions was investigated by Raman spectroscopy, using a Horiba Jobin Yvon Xplora plus. A microscope equipped with a 50 X lens was used to focus the laser beam (532 nm Ar-laser) on char particles, and the Raman spectra were taken randomly for each sample. The diameter of the laser spot on char surface was around 1 μm, much larger than the carbon microcrystals, thus providing the structural data of a large number of micro-crystallites [29]. For each char sample, Raman spectra of three particles were randomly recorded in the wavenumber range of 500-2,500 cm^{-1}. The acquisition time for each spectrum was 3 min. Furthermore, the carbon structure of chars was analyzed by X-ray diffraction (XRD) using a Rigaku Ultima IV X-ray diffractometer. The X-ray patterns were recorded with a steps-canning method in the range of 2θ=10-90° at a rate of 3°/min.

RESULTS AND DISCUSSION

1. Effect of Pressure on Morphology and Physical Structure of Char

The yield of volatile matter during pressurized entrained-flow pyrolysis is illustrated in Fig. 2. The volatile matter yield decreased with pyrolysis pressure at all pyrolysis temperatures studied. The changes in the volatile matter yield in the pressure range of 0.1-1.0 MPa agreed with the results reported by Niksa [36] and Tomeczek and Gil [37]. The high volatiles release at 0.1 MPa suggested

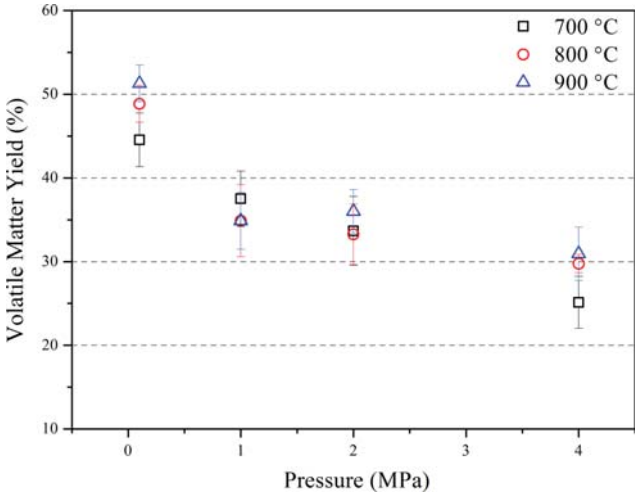

Fig. 2. Volatile matter yield during pyrolysis of coal as a function of pressure.

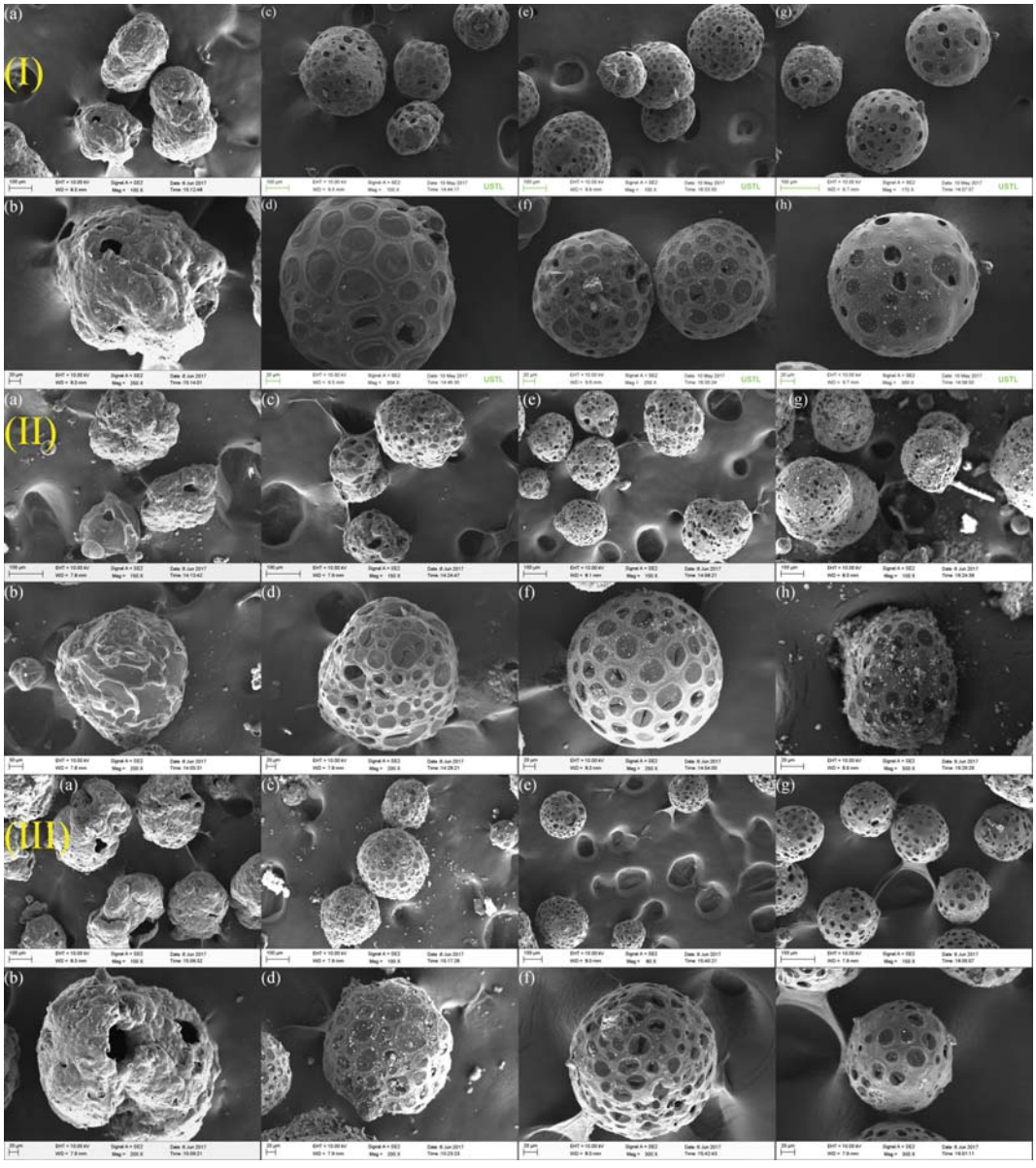

Fig. 3. Scanning electron microscopy (SEM) images of chars prepared at (I) 700 °C; (II) 800 °C; and (III) 900 °C and pressures of ((a), (b)) 0.1 MPa; ((c), (d)) 1.0 MPa; ((e), (f)) 2.0 MPa; ((g), (h)) 4.0 MPa, where (a) and (b), (c) and (d), (e) and (f), (g) and (h) show different magnifications of the same sample.

that the internal particle pressure that determined the chemical reaction rates of volatiles and volatile mass transport exceeded the reactor pressure [37]. The decrease in the volatile yields at higher pressures can be explained by the effect of pressure on vapor-liquid equilibrium and mass transport within the char particle [38]. The tar from bituminous coal usually contains compounds with a wide distribution of molecular weights. At elevated pressures, the vapor pressure of tar precursors with high molecular weight was not sufficient to overcome the particle exterior pressure. Thus, these tar precursors were retained in char, leading to a lower yield of volatiles at elevated pressures [12]. The mass transport of volatiles to the particle surface was also suppressed at higher pressures, resulting in lower volatile matter yields [20].

The SEM images of chars prepared under different experimental conditions are shown in Fig. 3. It can be seen that the morphology of char particles changed dramatically at elevated pressures. At all temperatures studied, the chars produced at atmospheric pressure had an irregular shape and showed signs of particle softening under single particle fast pyrolysis conditions [39]. The formation of large blow holes on the atmospheric chars was attributed to the rapid escape of volatiles from the softened particle as the internal particle pressure overcame the surface tension [12]. Fragmentation of char particles at atmospheric pressure was believed to be caused by fast heating rate and the escape of volatile from the particle during devolatilization.

Apparent changes were observed in the morphology of chars prepared at high pressures compared with those of atmospheric chars. Blow holes and fragmentation of char particles were not observed

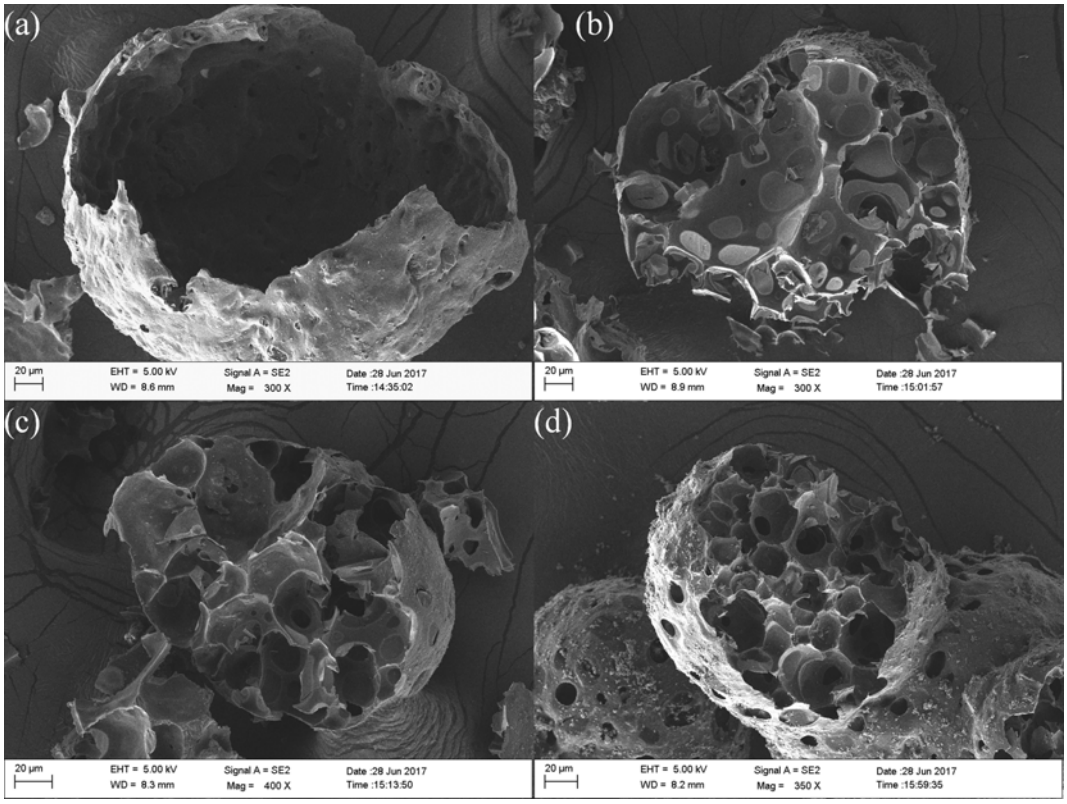

Fig. 4. SEM images showing the internal structures of char particles as a function of pressure: (a) 0.1 MPa, (b) 1.0 MPa, (c) 2.0 MPa, (c) 4.0 MPa.

in high-pressure chars. With increasing pyrolysis pressure, an intense bubble formation was observed under particle surface, implying a thin exterior wall [12]. The bubbles grew large during the plastic stage of coal devolatilization to form larger and hollow char particles [40]. Solid char particles with dense structures were not observed at elevated pressures, suggesting that the fraction of Group III chars was negligible [22].

To gain more insight into the internal structure, some char particles were crushed intentionally and subjected to SEM analysis (Fig. 4). The chars prepared at atmospheric pressure showed a cenospheric structure, while in the case of high-pressure chars bubble formation was observed. Bubbles were more evenly distributed in chars prepared at higher pressures. Also, the size of the bobbles in chars decreased at higher pressures and the bubble walls became thinner.

The physical process during char structure evolution at elevated pressure agreed well with the model proposed by Yu et al. [41]. The history of the swelling of the coal particle can be divided into three stages: pre-plastic, plastic, and resolidified [41]. The plastic stage and the bubble growth mechanism play a key role in the evolution of the char structure. At the early stages of devolatilization, protobubbles responsible for transportation of volatiles to char surface are formed. Potential bubble initiation sites are micropores in coal porous structure [42]. In the next stage, volatiles evolution and diffusion into the bubbles lead to the expansion of some bubbles near the center of the particle, while those near the surface of the particle collapse and release the volatiles. Further growth of the bubbles leads to the swelling of coal particle under pressure and a significant change in the morphology, leading to the formation of spherical particles. Unlike the atmospheric pressure conditions where the bubbles near the surface of the particle burst and released the volatiles, eventually forming cenospheric structure (Fig. 4(a)), the release of volatiles was limited under pressurized conditions due to the lower partial pressure of volatiles compared with the particle exterior pressure, resulting in lower volatile matter yields at higher pressures as shown in Fig. 2. As a result, the bubbles inside the particle further coalesced and grew into chars with a foam structure. Development of bubble structure may lead to a higher porosity of chars at elevated pressures [43]. The size and distribution of the bubbles depended on the pyrolysis pressure. Higher pressures resulted in a uniform distribution of smaller bubbles inside the particle by limiting the bubble growth (Fig. 4(d)), while lower pressures allowed coalescence and growth of the bubbles to a larger size, where they were unevenly distributed (Figs. 4(b) and 4(c)). The final structure of the char depended on the stage at which the particle was resolidified [41].

The changes in the physical structure of chars in relation to pyrolysis pressure are shown in Table 3. Chars prepared at 900 °C were mainly composed of mesopores with average diameters of 8.41-12.67 nm. With elevating the pressure from 0.1 MPa to 1.0 MPa, the N_2 surface area of chars increased by a factor of 9. However, a decreasing trend occurred with further increasing pressure to 4.0 MPa. The total pore volume of the chars followed a similar trend (Table 3). Roberts et al. [25] observed that for chars prepared under pressurized entrained-flow conditions, the highest surface area was obtained at 10 atm. Howaniec [15] reported that the chars pre-

Table 3. Structural properties of porous chars measured by nitrogen adsorption at 77 K

Sample	BET specific surface area (m^2/g)	Total pore volume (cm^3/g)	Average pore diameter (nm)
900 °C-0.1 MPa	2.44	0.007	11.93
900 °C-1.0 MPa	22.31	0.047	8.41
900 °C-2.0 MPa	5.91	0.019	12.67
900 °C-4.0 MPa	6.28	0.015	9.66

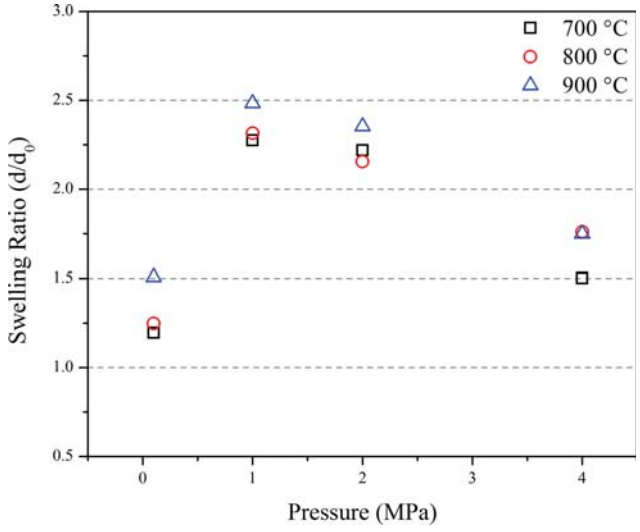

Fig. 5. Swelling ratios of chars as a function of pyrolysis pressure and temperature.

pared at 3.0 MPa had the highest surface area. In contrast, Zeng and Fletcher [12] found that the chars generated at higher pressures had the least developed pore structure.

The swelling of chars during pyrolysis may influence the subsequent reactivity during gasification or combustion [44]. As shown in Fig. 5, the highest swelling ratio of chars was obtained at 1.0 MPa. Two competing phenomena may affect the swelling properties of chars at elevated pressures. The enhanced fluidity of char and the yield of light gases (due to secondary pyrolysis reactions) led to a higher bubble growth rate, enhancing the particle swelling [22]. On the other hand, the higher external pressure exerted a force, restraining the bubble growth and decreasing the particle swelling [12]. These competing phenomena led to an optimum pressure of 1.0-1.5 MPa at which the highest swelling was obtained. These results are in agreement with those reported by Yu et al. [22, 41] and Wu et al. [21]. The higher swelling of char at 1.0 MPa enhanced the pore structure development, as shown in Table 3.

2. Effect of Pressure on the Chemical Structure of Char

Fig. 6 shows the IR spectra of chars as a function of pressure and temperature. With increasing pyrolysis pressure, a significant decrease in the intensity of the bands in 3,600-3,000 cm^{-1} (-OH), 3,000-2,800 cm^{-1} (C-H), 1,740-970 cm^{-1} (C=O, C=C, O-CH_3, C-O), and 900-500 cm^{-1} (C-H and C-C) regions occurred. These changes indicated the decomposition of functional groups during pyrolysis [45,46], which resulted in the formation of light gases.

The decrease in the intensity of bands in the 3,600-3,000 cm^{-1} (-OH) region indicated the loss of phenolic and alcoholic groups at elevated pressures. The decrease in intensity of bands in the 3,000-2,800 cm^{-1} (C-H) region corresponding to alkyl and aliphatic hydrogen groups suggested that methyl radicals were removed from the substituted aromatic rings, which may contribute to the generation of methane. The decrease in the intensity of bands in the 1,740-970 cm^{-1} region (C=O, C=C, O-CH_3, C-O) indicated the decomposition of oxygen-containing functional groups [47]. The decrease in O-CH_3 groups resulted in the formation of CH_4, while C-O decomposition contributed to the formation of CO and CO_2. The loss of C-H and C-C bands in the 900-500 cm^{-1} region suggested that changes in aromatic hydrogen structures occurred and fused rings may have formed at higher pyrolysis pressures and temperatures [47]. As discussed above, higher pressure decreased the volatile matter release during pressurized pyrolysis, which was mainly attributed to the retention of high molecular weight tar precursors in char, owing to the vapor-liquid equilibrium effects. The FTIR

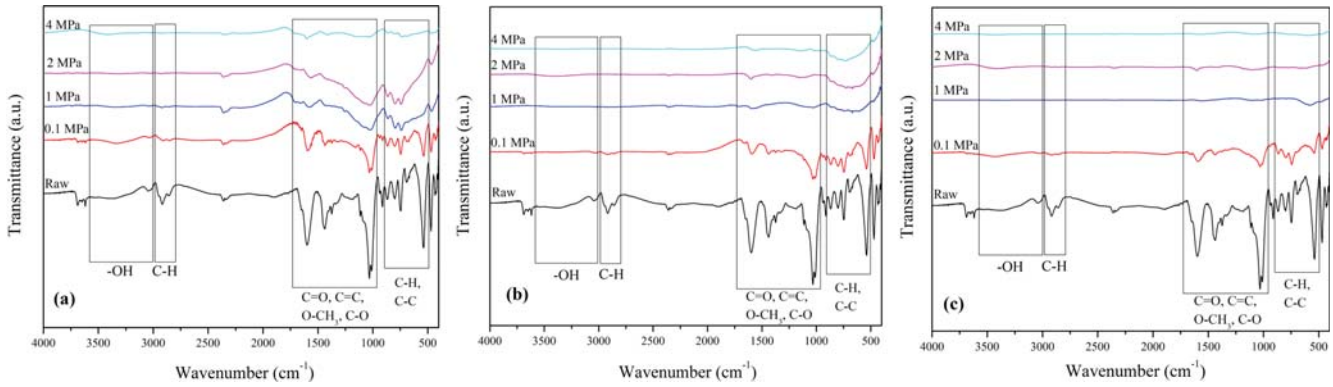

Fig. 6. FTIR spectra of the raw coal and chars from atmospheric and pressurized pyrolysis of coal: (a) 700 °C, (b) 800 °C, (c) 900 °C.

results indicated that the decomposition of functional groups such as -OH, C-H, O-CH_3, and C-O in coal structure was not hindered at elevated pressures, possibly due to lower bond energies of these groups, which were easily overcome at higher temperatures. Similar results were reported by Li et al. [45]. The decomposition of these functional groups resulted in the formation of light gases, predominantly CH_4, CO, H_2, and CO_2.

3. Effect of Pressure on Carbon Structure of Char

The Raman spectra of coal chars, which were prepared under various experimental conditions, were analyzed and deconvoluted into five bands. The Raman spectrum of pure graphite consists of a strong band at around 1,580 cm^{-1} (G band) [48]. In case of coal char, additional bands appear at around 1,350 (D1), 1,620 (D2), 1,530 (D3), and 1,150 (D4) cm^{-1} on the Raman spectra [29,49,50].

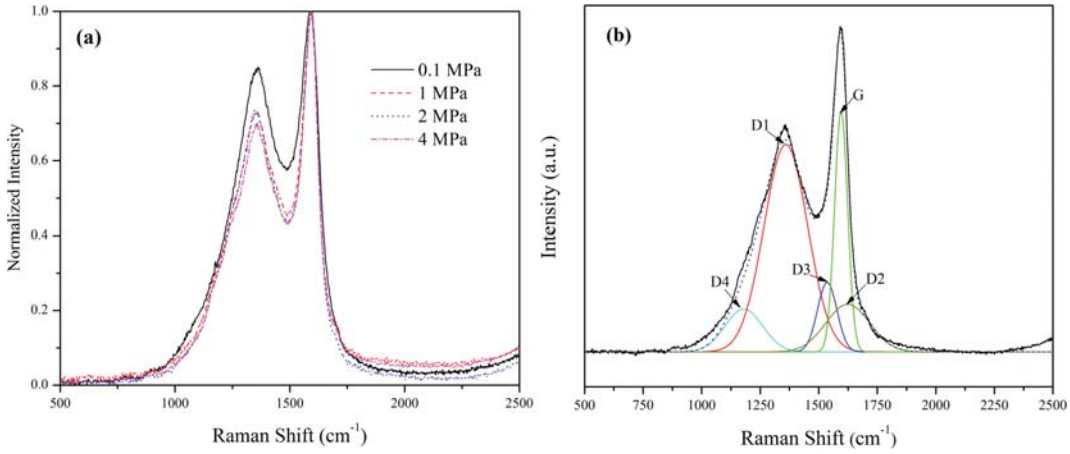

Fig. 7. (a) Typical normalized first-order Raman spectra of coal char as a function of pressure; (b) typical curve-fitting analysis of Raman spectra of coal chars.

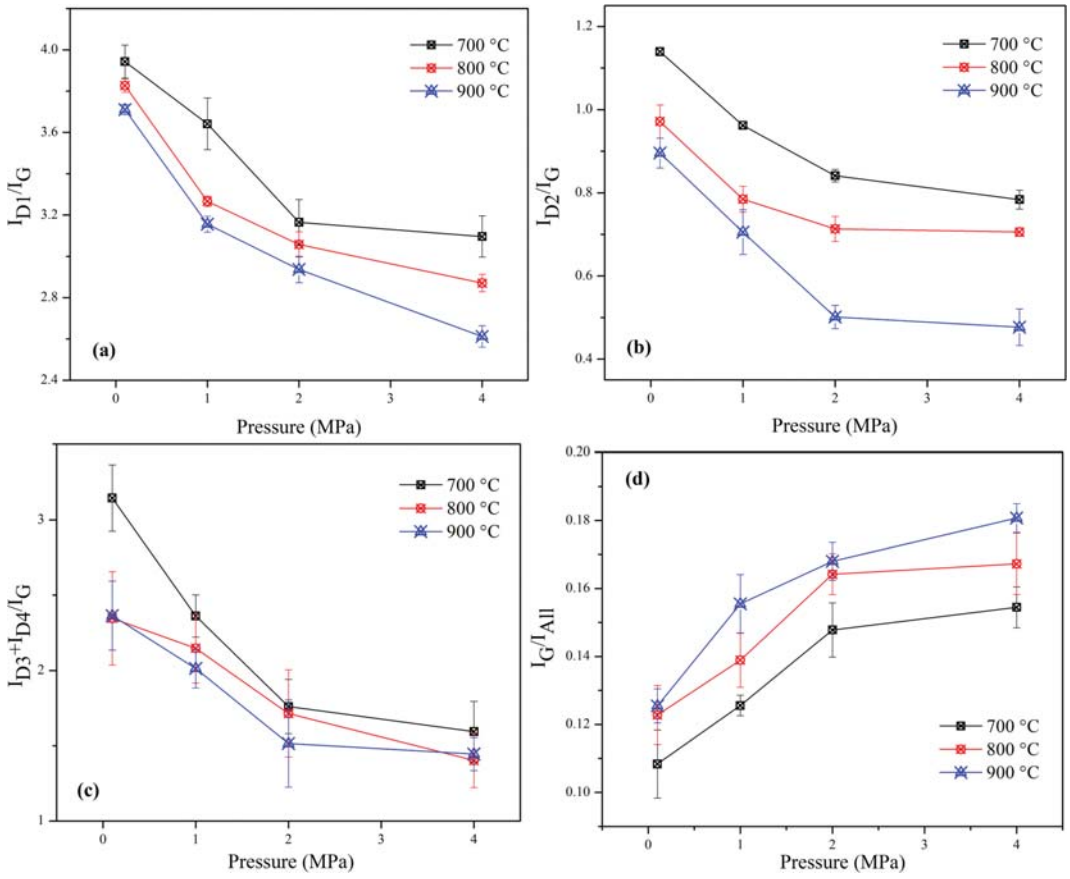

Fig. 8. Variation of band area ratios obtained from curve-fitting analysis of Raman spectra of chars as a function of pressure: (a) I_{D1}/I_G, (b) I_{D2}/I_G, (c) I_{D3+D4}/I_G, (d) I_G/I_{All}.

The D1 band may be attributed to the defects in graphene layers [51] and represents aromatic clusters with more than six rings [52]. The D2 band may be attributed to the disordered graphitic structures. The D3 band corresponds to the functional groups and organic molecules and is commonly seen in Raman spectra of poorly ordered chars [29,51]. The D4 band is attributed to $C_{aromatic}$-C_{alkyl} and aromatic (aliphatic) ethers [52].

Fig. 7(a) shows normalized Raman spectra of 700 °C chars as a function of pyrolysis pressure. Typical curve-fitting analysis results are illustrated in Fig. 7(b) with R^2=0.9984. Fig. 7(a) shows that the G band was stronger than the D1 band in all samples, indicating that a higher carbon order was achieved at elevated pressures. The D2, D3, and D4 bands had lower intensities compared with D1 and G bands, suggesting the presence of amorphous carbon in the char structure. In this study, the ratios of the integrated band areas were used as parameters to investigate the changes in carbon order of the char as a function of pressure.

Fig. 8 shows the band area ratios of I_{D1}/I_G, I_{D2}/I_G, I_{D3+D4}/I_G, and I_G/I_{All} as a function of pyrolysis pressure. As seen, the I_{D1}/I_G, I_{D2}/I_G, and I_{D3+D4}/I_G ratios decreased at elevated pressures, while an increasing trend was observed for I_G/I_{All}. The decrease in I_{D1}/I_G suggests that the average planar size of the graphitic micro-crystallites was increased [53]. The higher I_{D3+D4}/I_G ratio at elevated pyrolysis pressures indicates that the organic structures and functional groups were removed and the order of carbon structure was increased. This was also evident by higher I_G/I_{All} ratios [29]. These results are in good agreement with the FTIR results discussed above.

Fig. 9 shows the changes in $(I_{D2}+I_{D3})/I_{D1}$ ratio in relation to pyrolysis pressure. The $I_{D2}+I_{D3}$ bands were attributed to the amorphous carbon with small aromatic rings (3-5 rings), while I_{D1} represents developed aromatic systems containing more than six rings [54,55]. Thus, $(I_{D2}+I_{D3})/I_{D1}$ reflects the ratio of small to large aromatic systems. This ratio decreased in chars prepared at higher pressures, suggesting that larger aromatic ring systems were formed, owing to the hindering effect of pressure on the release of high-molecular-weight tar precursors [12]. At elevated pressures, aromatic tar precursors with lower molecular weight were removed, while those with high molecular weight were retained in the char.

The XRD analysis was carried out to gain a better understanding of the changes in the carbon order of chars. The XRD patterns of chars are shown in Fig. 10. At all temperatures studied, the intensity

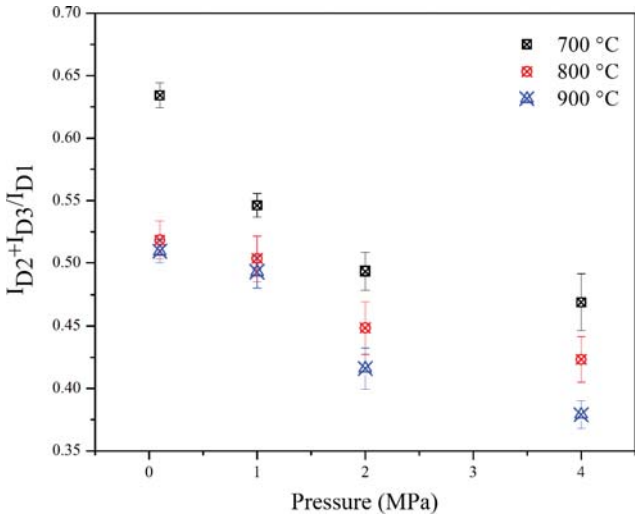

Fig. 9. Integrated Raman $(I_{D2}+I_{D3})/I_{D1}$ band area ratio as a function of pressure.

of the (002) peak at around 2θ=26.6° corresponding to the graphitic structures increased with pyrolysis pressure, indicating a better lattice structure and a higher degree of carbon order in the chars obtained at elevated pressures [45]. The XRD results were consistent and showed a good agreement with Raman spectroscopy analysis results (Fig. 8). The XRD peaks assigned to (100) and (101) peaks corresponding to in-plane reflections were also detected [56]. Al- though a higher carbon order was obtained for chars prepared at elevated pressures, the XRD and Raman spectroscopy results indicate that the char samples contained a significant amount of amorphous carbon.

The changes in the carbon structure of char samples as a function of pyrolysis pressure was further studied by analyzing the XRD patterns using Debye-Scherrer equations to obtain the structural parameters [57]:

$$L_c = \frac{0.9\lambda}{\beta_{002}\cos\theta_{002}} \quad (1)$$

$$L_a = \frac{1.94\lambda}{\beta_{100/101}\cos\theta_{100/101}} \quad (2)$$

$$n = \frac{L_c}{d_{002}} \quad (3)$$

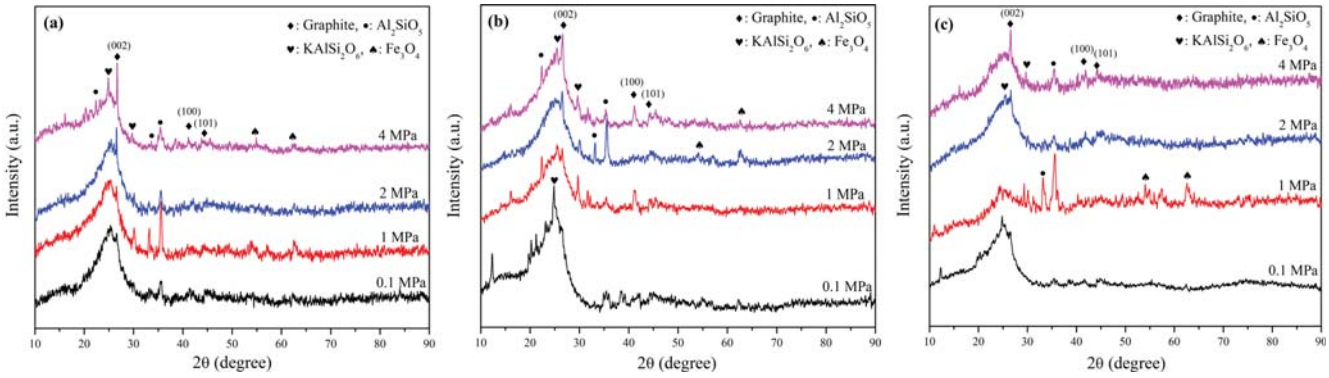

Fig. 10. XRD patterns of the chars as a function of pressure: (a) 700 °C, (b) 800 °C, (c) 900 °C.

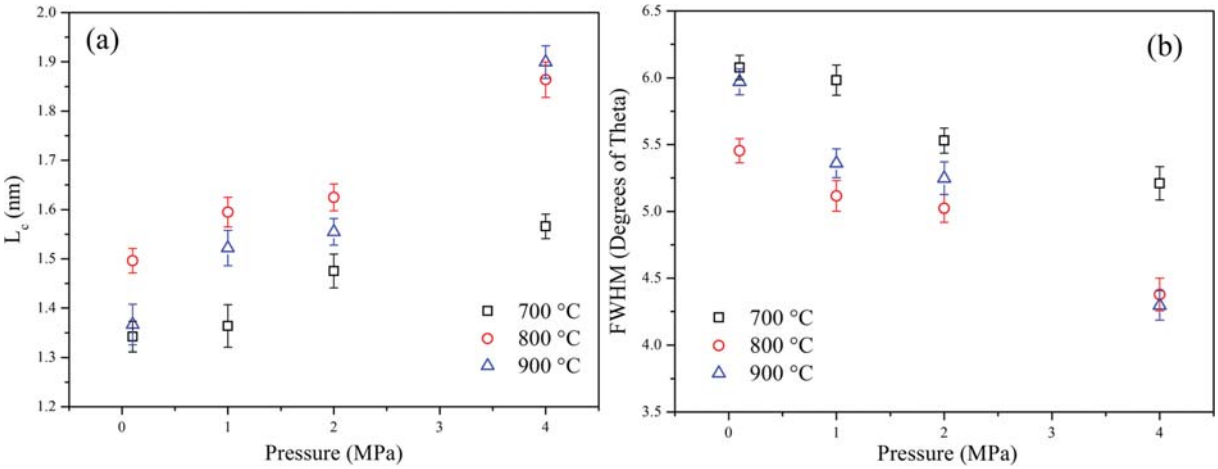

Fig. 11. Changes of (a) L_c and (b) FWHM of coal char as a function of pyrolysis pressure.

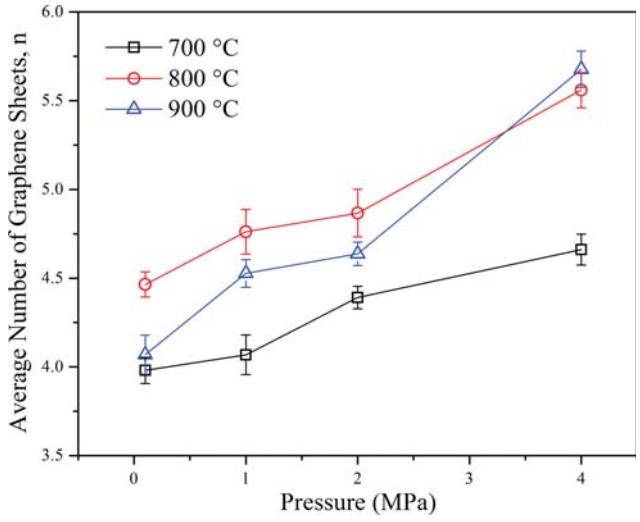

Fig. 12. Change of the average number of graphene sheets of chars with pyrolysis pressure.

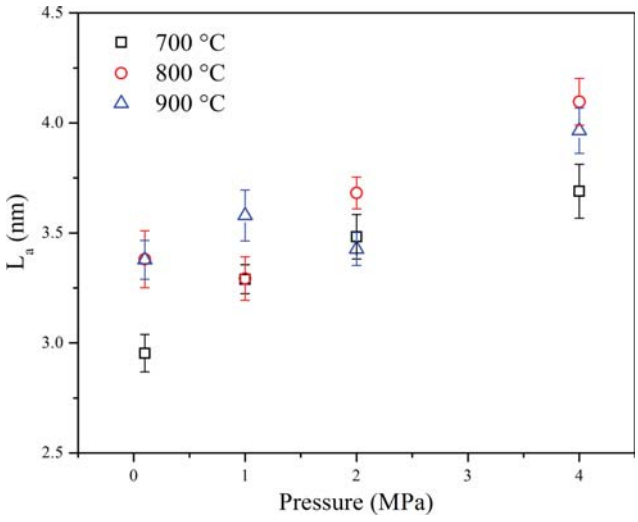

Fig. 13. Changes of L_a of coal char as a function of pyrolysis pressure.

where L_c is the stacking height, L_a is the lateral size of the graphitic structures, β is the full-width at half maximum (FWHM in radians of θ), λ is the wavelength of the X-ray, n is the number of graphene sheets, and d is the interlayer spacing. The FWHM values were obtained by curve-fitting analysis using the commercially available OriginPro program. The Debye-Scherrer equations are most suitable for calculation of L_c and L_a in highly graphitized carbon but may be used as an estimate of carbon order in turbostratic carbons such as coal char [57,58].

Fig. 11(a) shows the changes of the stacking height, L_c, of coal chars in relation to the pyrolysis pressure. In general, the values of L_c increased at elevated pressures and ranged between 1.34-1.89 nm in the char samples studied. The FWHM values of the chars show an opposite trend to that of L_c with increasing pyrolysis pressure (Fig. 11(b)). The interlayer spacing in char samples was calculated using the Bragg's Law and ranged between 3.34-3.37 Å, which were similar to the typical graphitic dimensions of 3.35 Å [57]. The observation that the interlayer spacing, d_{002}, did not change during the heat treatment was also reported by Feng et al. [59]. The average number of graphene sheets in chars increased with pyrolysis pressure and ranged between 3.98 and 5.68, as shown in Fig. 12, indicating a higher degree of carbon order at elevated temperatures.

The changes of L_a with pyrolysis pressure are shown in Fig. 13. Similar to L_c, a monotonic increase in L_a was observed with increasing pyrolysis pressure. The L_a values for chars ranged between 2.95 and 4.09 under the present experimental conditions. These results indicated that the stacking height and lateral size of the graphitic structures of the chars increased at elevated pressures, which was accompanied by about 43% increase in the number of graphene sheets. The increase of van der Waals forces between the layers may be responsible for the growth of the carbon layer plane [60]. Larger L_c and L_a led to the increase in the fraction of ordered carbon in chars at elevated pressures.

4. Implications of Potential Applications of Porous Char

The unique morphology and physiochemical structure of coal chars obtained from pressurized pyrolysis make them suitable as

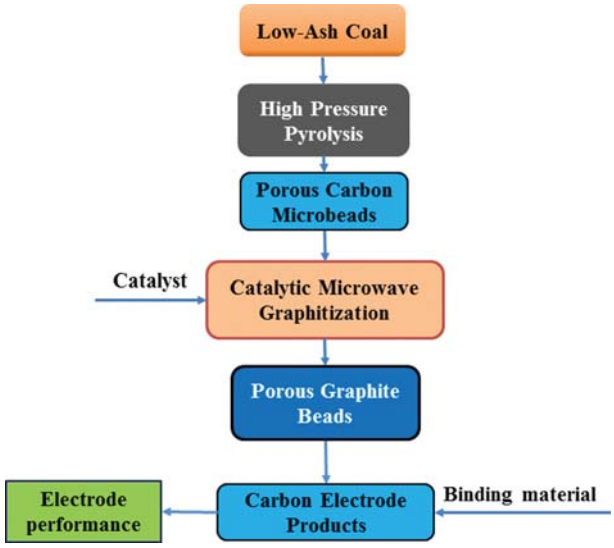

Fig. 14. The potential application of chars derived from pressurized pyrolysis of coal.

precursors for the production of advanced carbon materials. The implications of potential applications of chars derived from high-pressure pyrolysis are illustrated in Fig. 14. One potential pathway is the low-temperature catalytic graphitization of chars for converting the spherical char particles into graphite microbeads (GMBs). Low-temperature graphitization of char can be realized under microwave at a relatively low temperature as an alternative and energy-efficient graphitization method [61,62]. GMBs may find broad applications as precursors for anode materials in Li-ion batteries [63] as well as high-performance carbon materials [64]. The production of low-cost coal-based carbon materials with unique morphology and structure may pave the way for an alternative and efficient utilization of abundant coal resources. The precise economic evaluation of the proposed process has not been realized at this stage, but requires a comprehensive energy evaluation and techno-economic analysis of the process by considering several cost factors such as total capital, operation and maintenance, labour, coal, and total variable costs, as well as the scale and heat energy requirements of the pyrolysis reactor, water consumption, electricity, capital depreciation, taxes, insurance, and the cost of catalyst for low-temperature graphitization of carbon microbeads [65,66].

CONCLUSIONS

The effect of pressure on the structural evolution of coal char during fast pressurized entrained-flow pyrolysis was systematically investigated. The results showed that pyrolysis pressure had a profound impact on the morphology, swelling, internal structure, as well as the carbon structure of chars. The following conclusions were drawn:

1) Pyrolysis pressure had a significant influence on the volatile matter yield and the morphology of chars. The swelling of chars in- creased at elevated pressures and reached the highest value at 1.0 MPa.

2) The specific surface area and total pore volume of chars increased with pressure and reached the maximum value at 1.0 MPa, and decreased thereafter. This trend was in good agreement with the changes of swelling ratio of chars, indicating that pressure enhanced the development of the porous structure of char.

3) Raman spectroscopy results showed that with increasing of char preparation pressure, the structural defects in carbon structure, organic matrix, and functional groups in char were removed and the amorphous carbon was turned into a more ordered structure.

4) The XRD results showed a good agreement with the Raman spectroscopy analysis data. The interlayer spacing, d_{002}, in chars remained relatively unchanged at elevated pressures. However, the stacking height, the lateral size of the graphitic structures, and the average number of graphene sheets in chars increased with pyrolysis pressure, indicating an increase in the fraction of ordered carbon in chars.

ACKNOWLEDGEMENTS

This study was supported by the National Natural Science Foundation of China (21676132 and 21476100) and Department of Education Science and Technology Key Research Project, Liaoning Provincial of China (2016TSZD03).

REFERENCES

1. T. Das, H. Chauhan, S. Deka, S. Chaudhary, R. Boruah and B. K. Saikia, *Micropor. Mesopor. Mater.*, **253**, 80 (2017).
2. R. Ye, Z. Peng, A. Metzger, J. Lin, J. A. Mann, K. Huang, C. Xiang, X. Fan, E. L. G. Samuel, L. B. Alemany, A. A. Martí and J. M. Tour, *ACS Appl. Mater. Interf.*, **7**, 7041 (2015).
3. K. Moothi, S. E. Iyuke, M. Meyyappan and R. Falcon, *Carbon*, **50**, 2679 (2012).
4. Q. Zhou, Z. Zhao, Y. Zhang, B. Meng, A. Zhou and J. Qiu, *Energy Fuels*, **26**, 5186 (2012).
5. R. Ye, C. Xiang, J. Lin, Z. Peng, K. Huang, Z. Yan, N. P. Cook, E. L. G. Samuel, C.-C. Hwang, G. Ruan, G. Ceriotti, A.-R. O. Raji, A. A. Martí and J. M. Tour, *Nature Commun.*, **4**, 2943 (2013).
6. T. Liu, R. Luo, W. Qiao, S.-H. Yoon and I. Mochida, *Electrochim. Acta*, **55**, 1696 (2010).
7. A. J. Smith, M. J. MacDonald, L. D. Ellis, M. N. Obrovac and J. R. Dahn, *Carbon*, **50**, 3717 (2012).
8. A. C. Rady, S. Giddey, A. Kulkarni, S. P. S. Badwal and S. Bhattacharya, *Electrochim. Acta*, **178**, 721 (2015).
9. A. C. Rady, S. Giddey, A. Kulkarni, S. P. S. Badwal, S. Bhattacharya and B. P. Ladewig, *Appl. Energy*, **120**, 56 (2014).
10. J. McDonald-Wharry, M. Manley-Harris and K. Pickering, *Carbon*, **59**, 383 (2013).
11. D. J. Harris, D. G. Roberts and D. G. Henderson, *Fuel*, **85**, 134 (2006).
12. D. Zeng and T. H. Fletcher, *Energy Fuels*, **19**, 1828 (2005).
13. T. P. Griffin, J. B. Howard and W. A. Peters, *Fuel*, **73**, 591 (1994).
14. H. Y. Cai, A. J. Güell, I. N. Chatzakis, J. Y. Lim, D. R. Dugwell and R. Kandiyoti, *Fuel*, **75**, 15 (1996).
15. N. Howaniec, *Fuel*, **172**, 118 (2016).
16. V. Seebauer, J. Petek and G. Staudinger, *Fuel*, **76**, 1277 (1997).
17. C. L. Sun, Y. Q. Xiong, Q. X. Liu and M. Y. Zhang, *Fuel*, **76**, 639

(1997).
18. Y. Yun and G.-B. Lee, *Korean J. Chem. Eng.*, **16**, 798 (1999).
19. F. Jiménez, F. Mondragón and D. López, *J. Anal. Appl. Pyrol.*, **95**, 164 (2012).
20. C. W. Lee, A. W. Scaroni and R. G. Jenkins, *Fuel*, **70**, 957 (1991).
21. H. Wu, G. Bryant, K. Benfell and T. Wall, *Energy Fuels*, **14**, 282 (2000).
22. J. Yu, D. Harris, J. Lucas, D. Roberts, H. Wu and T. Wall, *Energy Fuels*, **18**, 1346 (2004).
23. D. Zeng, M. Clark, T. Gunderson, W. C. Hecker and T. H. Fletcher, *Proc. Combust. Inst.*, **30**, 2213 (2005).
24. A. Tremel, T. Haselsteiner, M. Nakonz and H. Spliethoff, *Energy*, **45**, 176 (2012).
25. D. G. Roberts, D. J. Harris and T. F. Wall, *Energy Fuels*, **17**, 887 (2003).
26. X. Gong and S. Zhang, *J. Anal. Appl. Pyrol.*, **127**, 170 (2017).
27. V. P. Chabalala, N. Wagner and S. Potgieter-Vermaak, *Fuel Process. Technol.*, **92**, 750 (2011).
28. A. Zaida, E. Bar-Ziv, L. R. Radovic and Y.-J. Lee, *Proc. Combust. Inst.*, **31**, 1881 (2007).
29. C. Sheng, *Fuel*, **86**, 2316 (2007).
30. J. Xiao, F. Li, Q. Zhong, J. Huang, B. Wang and Y. Zhang, *J. Anal. Appl. Pyrol.*, **117**, 64 (2016).
31. Z. Wu, S. Wang, J. Zhao, L. Chen and H. Meng, *Fuel*, **171**, 65 (2016).
32. S. Li, X. Chen, A. Liu, L. Wang and G. Yu, *Bioresour. Technol.*, **179**, 414 (2015).
33. S. Li, X. Chen, A. Liu, L. Wang and G. Yu, *Bioresour. Technol.*, **155**, 252 (2014).
34. A. Haider and O. Levenspiel, *Powder Technol.*, **58**, 63 (1989).
35. D. Reichel, S. Siegl, C. Neubert and S. Krzack, *Fuel*, **158**, 983 (2015).
36. S. Niksa, *Combust. Flame*, **100**, 384 (1995).
37. J. Tomeczek and S. Gil, *Fuel*, **82**, 285 (2003).
38. K. Maliutina, A. Tahmasebi and J. Yu, *Bioresour. Technol.*, **256**, 160 (2018).
39. H. Y. Park and D. H. Ahn, *Korean J. Chem. Eng.*, **24**, 24 (2007).
40. M. V. Gil, J. Riaza, L. Álvarez, C. Pevida, J. J. Pis and F. Rubiera, *Appl. Energy*, **91**, 67 (2012).
41. J. L. Yu, V. Strezov, J. Lucas, G. S. Liu and T. Wall, *Proc. Combust. Inst.*, **29**, 467 (2002).
42. D. R. Jenkins and M. R. Mahoney, *Fuel*, **153**, 585 (2015).
43. J. Yu, J. A. Lucas and T. F. Wall, *Prog. Energy Combust. Sci.*, **33**, 135 (2007).
44. V. Strezov, J. A. Lucas and T. F. Wall, *Fuel*, **84**, 1238 (2005).
45. C. Li, J. Zhao, Y. Fang and Y. Wang, *Energy Fuels*, **23**, 5099 (2009).
46. F. Meng, J. Yu, A. Tahmasebi, Y. Han, H. Zhao, J. Lucas and T. Wall, *Energy Fuels*, **28**, 275 (2014).
47. T. Yuan, A. Tahmasebi and J. Yu, *Bioresour. Technol.*, **175**, 333 (2015).
48. X. Zhu and C. Sheng, *Fuel Process. Technol.*, **91**, 837 (2010).
49. O. Beyssac, B. Goffé, J.-P. Petitet, E. Froigneux, M. Moreau and J.-N. Rouzaud, *Spectrochim. Acta A*, **59**, 2267 (2003).
50. Y. Yin, J. Zhang and C. Sheng, *Korean J. Chem. Eng.*, **26**, 895 (2009).
51. A. Sadezky, H. Muckenhuber, H. Grothe, R. Niessner and U. Pöschl, *Carbon*, **43**, 1731 (2005).
52. C.-Z. Li, *Fuel*, **86**, 1664 (2007).
53. F. Tuinstra and J. L. Koenig, *J. Chem. Phys.*, **53**, 1126 (1970).
54. Y. Bai, Y. Wang, S. Zhu, F. Li and K. Xie, *Energy*, **74**, 464 (2014).
55. X. Li, J.-i. Hayashi and C.-Z. Li, *Fuel*, **85**, 1700 (2006).
56. D. K. Singh, P. K. Iyer and P. K. Giri, *Diam. Relat. Mater.*, **19**, 1281 (2010).
57. B. Sakintuna, Y. Yürüm and S. Çetinkaya, *Energy Fuels*, **18**, 883 (2004).
58. K. Gurudatt and V. S. Tripathi, *Carbon*, **36**, 1371 (1998).
59. B. Feng, S. K. Bhatia and J. C. Barry, *Carbon*, **40**, 481 (2002).
60. H. Fujimoto and M. Shiraishi, *Carbon*, **39**, 1753 (2001).
61. T. Kim, J. Lee and K.-H. Lee, *RSC Adv.*, **6**, 24667 (2016).
62. K. S. Yang, Y. J. Yoon, M. S. Lee, W. J. Lee and J. H. Kim, *Carbon*, **40**, 897 (2002).
63. Y. Yang, Q. Lin, Y. Huang and D. Guo, *J. Anal. Appl. Pyrol.*, **91**, 310 (2011).
64. R. Moriyama, H. Kumagai, J. i. Hayashi, C. Yamaguchi, J. Mondori, H. Matsui and T. Chiba, *Carbon*, **38**, 749 (2000).
65. Y. Huang, W.-y. Li, G.-s. Wu, J. Feng and Q. Yi, *Energy Fuels*, **31**, 12977 (2017).
66. T. Hosseini, A. De Girolamo and L. Zhang, *Energy Fuels*, **32**, 3211 (2018).